



Present-Day Crustal Deformation of the Northwestern Tibetan Plateau Based on InSAR Measurements

Guifang Zhang, Chunyan Qu *, Xinjian Shan, Xiaogang Song, Yingfeng Zhang and Yanchuan Li

State Key Laboratory of Earthquake Dynamics, Institute of Geology, China Earthquake Administration, Beijing 100029, China; gfzhang@ies.ac.cn (G.Z.)

* Correspondence: dqchuy@sohu.com

Abstract: In this study, The ENVISAT advanced synthetic aperture radar observations from 2003 to 2010 of a descending track covering an area of 100 km × 300 km were used to map the surface velocity field in northwestern Tibet. The derived line-of-sight (LOS) velocity map revealed that interseismic deformation was mainly located on the Altyn Tagh Fault (ATF) and other four immature subsidiary faults (i.e., Tashikule Fault, Muzitage-jingyuhe Fault, Heishibeihu Fault, and Woniuhu Fault). A 2D elastic screw dislocation model was used to interpret the interferometric synthetic aperture radar (InSAR) velocity profiles, which revealed the following results. (a) The oblique movement is partitioned between left-lateral slip at a rate of 6.3 ± 1.4 mm/y on the ATF and 5.9 ± 2.8 mm/y on the subsidiary faults. The low slip rate of the ATF indicates that the ATF does not drive the northeastward extrusion of material, with most of the extrusion occurring in the eastern interior of the plateau and the four subsidiary faults localizing the oblique convergence partitioned in the west. This can reasonably explain why catastrophic earthquakes and rapid slip do not occur all over along the ATF. (b) Based on the four subsidiary faults accommodating the oblique movement and the traces amalgamation with the EKLf (delineated Bayan Har plate boundary to the northeast), we concluded guardedly that the four subsidiary faults are the evolving plate boundary of the Bayan Har block to the northwest. (c) The Tanan top-up structure had an uplift rate of ~ 0.6 mm/y at the south of the Tarim Basin.

Keywords: crustal deformation; Tibetan Plateau; InSAR; displacement modeling



Citation: Zhang, G.; Qu, C.; Shan, X.; Song, X.; Zhang, Y.; Li, Y. Present-Day Crustal Deformation of the Northwestern Tibetan Plateau Based on InSAR Measurements. *Remote Sens.* **2023**, *15*, 5195. <https://doi.org/10.3390/rs15215195>

Academic Editor: Alex Hay-Man Ng

Received: 20 September 2023

Revised: 16 October 2023

Accepted: 24 October 2023

Published: 31 October 2023



Copyright: © 2023 by the authors. Licensee MDPI, Basel, Switzerland. This article is an open access article distributed under the terms and conditions of the Creative Commons Attribution (CC BY) license (<https://creativecommons.org/licenses/by/4.0/>).

1. Introduction

The Tibetan Plateau (TP) is a consequence of the collision between the Indian and Eurasian plates, which began approximately 50 million years ago. Continental collision has resulted in widely distributed block boundary deformation in the TP [1–3] with crustal shortening, thickening, and eastward extrusion [4,5]. Therefore, the understanding of crustal deformation processes and mechanisms is important for the evaluation of potential earthquakes.

The Altyn Tagh Fault (ATF), a lithospheric-scale boundary fault, is not only marked by its surface trace, but is also revealed by seismic reflection profiles and tomographic imaging [6–8]. The ATF has attracted broad attention because its slip rate is of great significance in understanding present-day crustal deformation in the northern TP. Late Quaternary slip rates have been reported along most of the ATF at both decadal and millennial timescales [9–18]. Previous tectonic deformation studies reported high slip rates of up to 20–30 mm/y. These results suggest the fast eastward movement of an effectively rigid Tibetan lithospheric block [5,19]. Subsequently, space geodesy techniques such as the global positioning system (GPS) and the interferometric synthetic aperture radar (InSAR) indicate that the ATF experiences slip at a decadal time scale of approximately 6–10 mm/y [9,14,15,20,21]. One reason for the slip rate discrepancies by nearly a factor of five may be the changes in the slip rate on the ATF over time [14]. How these changes

occur and their long-term impact on the TP deformation mode is not well understood. Understanding this problem requires detailed modern fault observations.

Other continental strike-slip faults, including the Kunlun, San Andreas, and North Anatolian faults, have experienced numerous catastrophic earthquakes. In contrast, only a minor level of seismicity has been detected by instrumental recordings along the entire active strike-slip ATF over nearly 100 years (Figure 1). Because no catastrophic earthquakes have occurred along the ATF, a high slip rate would accommodate a large part of the India–Asia convergence [11,22,23]. Conversely, a low ATF rate requires deformation to be distributed throughout the plateau. Consequently, questions remain as to whether subsidiary faults accommodate slip rates, highlighting the need for better quantification of slip rates on the ATF and its subsidiary faults.

Dynamic models of two major mechanisms have been proposed to explain the uplift and faulting behaviors of the TP: the block [5,19,22,24–26] and continuum [4,9,27,28] models. The block model considers the crust to be sliced into a limited number of blocks that are internally rigid and move relative to each other along their boundary faults [19,29]. It has been primarily applied to model the kinematics of deformation observed at the Earth's surface [30]. The continuum model attributes crustal deformation driven by a “soft” lithosphere to be broadly distributed even within blocks [27,31,32]. It unites kinematics and dynamics under the assumption that the deformation is controlled by the ductile properties of the lithosphere [33]. These models describe the motion and construction history of a plateau. Although the block and continuum models predict distinctly different deformation patterns and mechanical behaviors, the differences between their kinematics are ultimately gradational. As the block size decreases and the number of faults increases, the block model approaches the deformation of the continuum model, and the kinematic distinction between the two models becomes blurred [30]. Zhang et al. [2] analyzed the GPS velocities in Tibet and revealed that the deformation field was largely continuous. However, Meade [34] and Thatcher [35] interpreted the same dataset and found that the rigid block motion model still holds if the crust is subdivided into smaller blocks than previously envisioned. To date, crustal deformation studies have mostly concentrated on block boundary faults or fault zones within Tibet [15,36–40]. However, the May 2021 Mw 7.4 Maduo earthquake that occurred in the interior of the Bayanhar Block implies that the deformation of subsidiary faults within blocks cannot be neglected [18,41,42].

This study investigated the region located east of the junction zone, in the westernmost central segment of the ATF system, and the western segment of the eastern Kunlun Fault (EKLF) system. The geometric traces of subsidiary faults converge at the western end of the EKLF in this region. In previous studies, the Heishibeihu Fault (one of four subsidiary faults) was determined to be the northwestern margin of the Bayan Har block [43–45], which is considered to be the block with the most active boundaries in China. Compared with other broadly studied faults (ie., EKLF, Ganzi-yushu-Xianshuihe fault and Longmenshan fault) around the Bayan Har block [18,46,47], its northwestern margin faults have not been given the same attention and the relevant references can almost not be retrieved. Interferometric synthetic aperture radar (InSAR), as a geodesy-based powerful monitoring tool, is used to map spatially continuous surface deformation at a resolution ranging from meters to hundreds of meters. The increasing SAR images enable substantial improvements in precision of displacement measurements and provide routine observations of low-amplitude deformation associated with tectonic plate motions and active fault systems over a wide range of spatial. In this study, we used InSAR observations from 2003 to 2010 on one descending ENVISAT track with a spatial coverage between 84°E and 86°E (Figure 1) to map the surface motions and gradients of an area of over 100 km × 300 km. We investigated the slip rates of ATF and subsidiary faults and further discussed the current deformation behavior of the TP. Our analysis suggests that the deformation mode of the TP is similar to the continuum deformation. The results of this study can be valuable for drawing the crustal structure of the TP and for insight into understanding the evolution process of the TP.

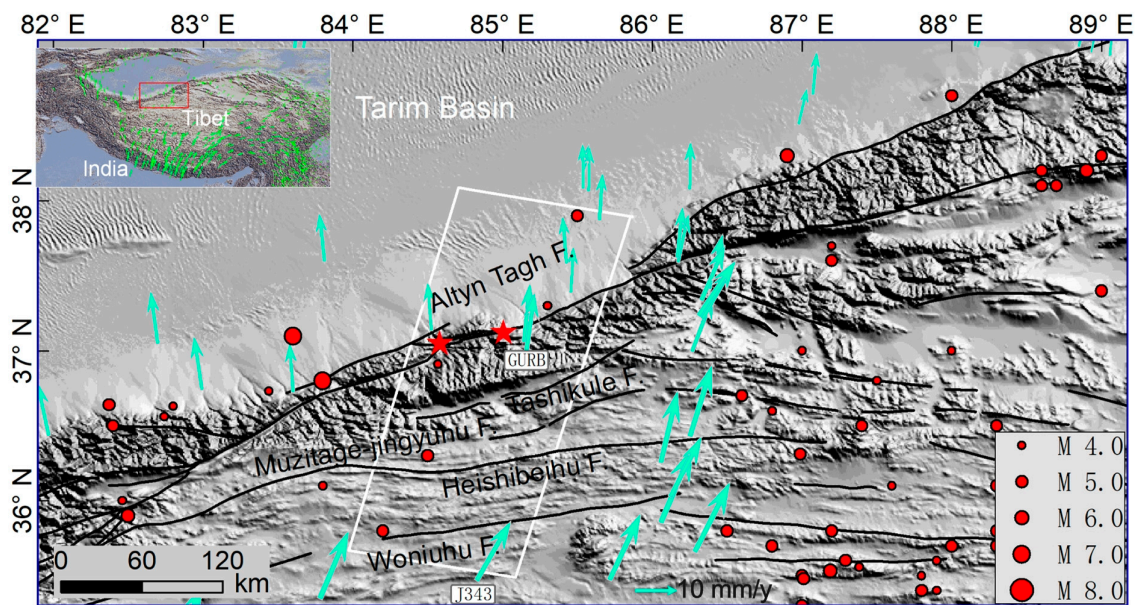


Figure 1. Tectonic setting of the ATF and four other faults in the study area. White box is the SAR coverage. Red dots are earthquakes with magnitudes >3.0 from 1966 to 2020 downloaded from <http://data.earthquake.cn/data/index.jsp> (accessed on 10 June 2020). Green arrows are GPS stations from Wang et al. [18] Red stars are two sub-branchpoints along the ATF. Black lines are active faults from Xu et al. [48].

2. Methods

2.1. InSAR Processing

2.1.1. ENVISAT Dataset

The ENVISAT archive dataset of descending track 391 from 2003 to 2010 was used to investigate the interseismic deformation of the study area (Figure 1). During the SAR data processing, multilook SAR images were generated 4 and 20 times in the range and azimuth directions, respectively. To resample a set of SLCs to a common reference SLC, all single-look complex images were registered to a single master image geometry based on the DEM. We compared the co-registration based on the digital elevation model (DEM) and coherence coefficient and found that the accuracy of co-registration in the range direction was greatly improved (detailed see Figure S1). In this study, single-look complex images were registered to a single master image geometry based on the DEM. Precise DORIS orbital data from the ENVISAT satellite provided by the European Space Agency were used for interferometric processing. Affected by complex terrain, permanently coherent pixels do not cover a sufficiently large area for the observation of interseismic deformation. Therefore, we first constructed interferometric pairs with large spatial (3000 d) and temporal (500 m) baselines. Then, we selected the pairs with a ratio over 0.4 and a coherence over 0.5 from all pixels of the image, such that the highly coherent pixels could cover a sufficiently large area. This method is useful for time-series deformation analyses of complex terrain areas. We constructed 164 differential pairs and formed a redundancy network of interferograms (Figure 2).

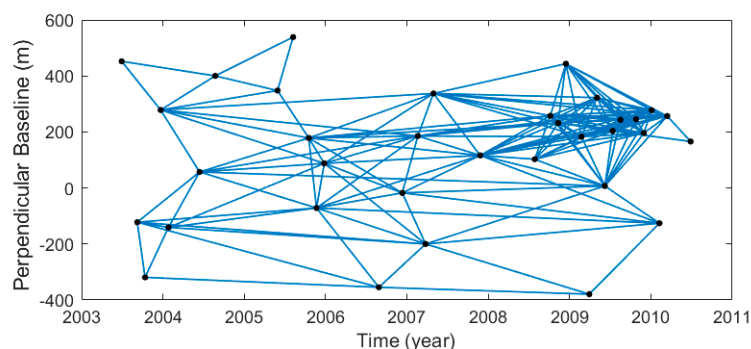


Figure 2. Network of SAR interferograms defined using spatial and temporal baseline constraints that ensure redundancy.

2.1.2. Multiple Error Correction

In order to construct a high accuracy velocity map, a series of refined data processing approaches was used to correct multiple errors. Taking account of the empirical method [49–51] may remove some displacement-related signals when deformation correlates with topography, which is the case for major topographic steps such as ATF. We used the predictive method [52–55] to correct the atmospheric delay using GACOS (<http://ceg-research.ncl.ac.uk/v2/gacos/> (accessed on 8 July 2016)) for InSAR [56] in the wrapped phase to prevent unwrapping errors. We removed the atmospheric delay from the original observations (Figure S2a) and obtained an atmospheric phase screen (APS)-corrected interferogram (Figure S2b). Profiles a and b in Figure S3 show the phase quantification of the original and APS-corrected interferograms. The atmospheric delay was mostly reduced across the ATF. However, in the presence of steep topography, interpolating weather model parameters between grid nodes at significantly different elevations can produce artifacts in phase-delay maps because the weather model must be extrapolated below the Earth’s surface. Artifacts were decreased by following local DEM error correction.

InSAR is limited by DEM errors, which can result both in phase discontinuities and in apparent decorrelation noise, especially in mountainous areas. Therefore, DEM error correction is particularly important in high-topography areas. In this study, the DEM errors were corrected (Figure S4) before unwrapping using the method described in [57]. Figure S4 demonstrates that DEM errors are larger in the presence of steep topography and display typical oblique striations at short wavelengths near the edges of sedimentary basins, where the phases are steeper. Sometimes, they exceed half a cycle, making phase unwrapping difficult in these areas. A comparison between the original and corrected differential interferograms shows that most of the residual topographic features were successfully corrected, and the local phase variability was significantly reduced. The DEM error correction before the unwrapping step can prevent unwrapping errors in steep topographic areas. Simultaneously, DEM error correction significantly reduces the noise in the wrapped phase for further processing.

The phase values in an interferogram are initially wrapped modulo $2k\pi$, and an unwrapping step during processing attempts to remove the $2k\pi$ ambiguity to produce a continuous map of phase values. The resulting interferogram often has unwrapping errors which appear as $2k\pi$ phase jumps in the presence of noise or no continuous spatial coverage. The phase closure technique [58] was used to identify the major unwrapping errors remaining in the interferograms. We only identified and corrected major unwrapping errors, small unwrapping errors were still present and were masked in succeeding processing (Figure S5).

Because of the imperfect knowledge on the state vector of the ENVISAT satellite, even after the effects of baseline separation have been removed, two or three orbital ramp cycles can remain in the long strips and more cycles can remain in long-wavelength ionospheric delay interferograms. Most previous studies individually estimated the orbital ramps on interferograms [59,60]. A linear approximation is typically sufficiently accurate

for short strips, whereas a quadratic approximation is required for long strips. Each acquisition was used to construct several interferograms; therefore, the orbital contribution to a single acquisition was estimated using the constraints from many interferograms. Biggs et al. [58] presented a network approach to empirically estimate the orbital error for each acquisition rather than for each interferogram. The network approach uses least squares inversion to find the best fitting simultaneous linear ramp at each acquisition and the static offset for each interferogram. This correction technique also accounts for other long-wavelength signals such as ionospheric and long-wavelength tropospheric contributions and orbital errors [58]. This method was used to remove the orbital ramps remaining in the interferograms (Figure S6).

2.2. Constructing the Line-of-Sight (LOS) Velocity Map

In this study, the Time Series InSAR with Atmospheric Estimation Model (TSInSAR-AEM), as proposed by Li et al. [61], was used to process the available error corrected SAR images. This technique is performed iteratively by way of a pixel-by-pixel temporal analysis to find a solution until convergence is achieved. Note, that is a component of non-linear surface motion. The nonlinear displacements are correlated both in space and in time, and we distinguished the nonlinear displacements by spatial and temporal filter from the thermal noise, which spatially and temporally decorrelated in the whole set of the unwrapped interferograms. The details can be found in Wen et al. [62] and Li et al. [61]. We constructed the LOS displacement of the study area based on unwrapped interferograms.

3. Results

3.1. LOS Velocity Field

To obtain high-coverage and high-accuracy InSAR velocity maps, we implemented a series of approaches to increase the signal-to-noise ratio. Co-registration based on the DEM can enhance the coherence of interferograms and decrease the influence of orbit errors on the range and clock drift [63,64]. Atmospheric delays and DEM error corrections were applied to the wrapped phase to reduce the phase variability and phase jumps before unwrapping. A global network orbital correction approach was applied to remove long-wavelength orbital errors, and a closed-loop network method was used to detect and correct phase-unwrapped errors. Using the approaches presented above, we constructed an LOS velocity map that sheds light on continental deformation.

The InSAR LOS velocity field (Figure 3a) shows a left-lateral slip deformation pattern across the ATF with a velocity difference of approximately 1.5–2.0 mm/y (Figure 3a,b). Two sub-branchpoints are located along the trace of the ATF (red stars in Figure 3): the Meletche outlet (western star) and Dalaku'an outlet (eastern star). Two thrust faults are located north of the ATF near the two sub-branch points. We obtained three LOS velocity profiles (CC', DD', and EE' in Figure 3a) paralleling the ATF. We compared the three profiles and found that the velocity was almost below zero near the sub-branchpoints, with larger values being farther from the sub-branchpoints. The velocity field also shows a pop-up belt between the two linear structures south of the Tarim Basin, as indicated by the arrows and dotted lines (Figure 3a,b,e). The two-line structure is referred to as the south-dipping Cherchenhe Fault and north-dipping Qiemo-Ruoqiang Fault [65,66], which control the development of the pop-up structure in the form of a facing-dipping structure. The velocity profiles indicate a slight gradient to the north of approximately 0.5 mm/y across the Cherchenhe Fault, and the velocity gradient across the Qiemo-Ruoqiang Fault was 0.6 mm/y. The rivers across the Qiemo-Ruoqiang Fault are straight and undeflected (Figure 3e), all of which show typical characteristics associated with a thrust fault. Thus, we inferred that the Qiemo-Ruoqiang Fault is dominated by pure dip-slip.

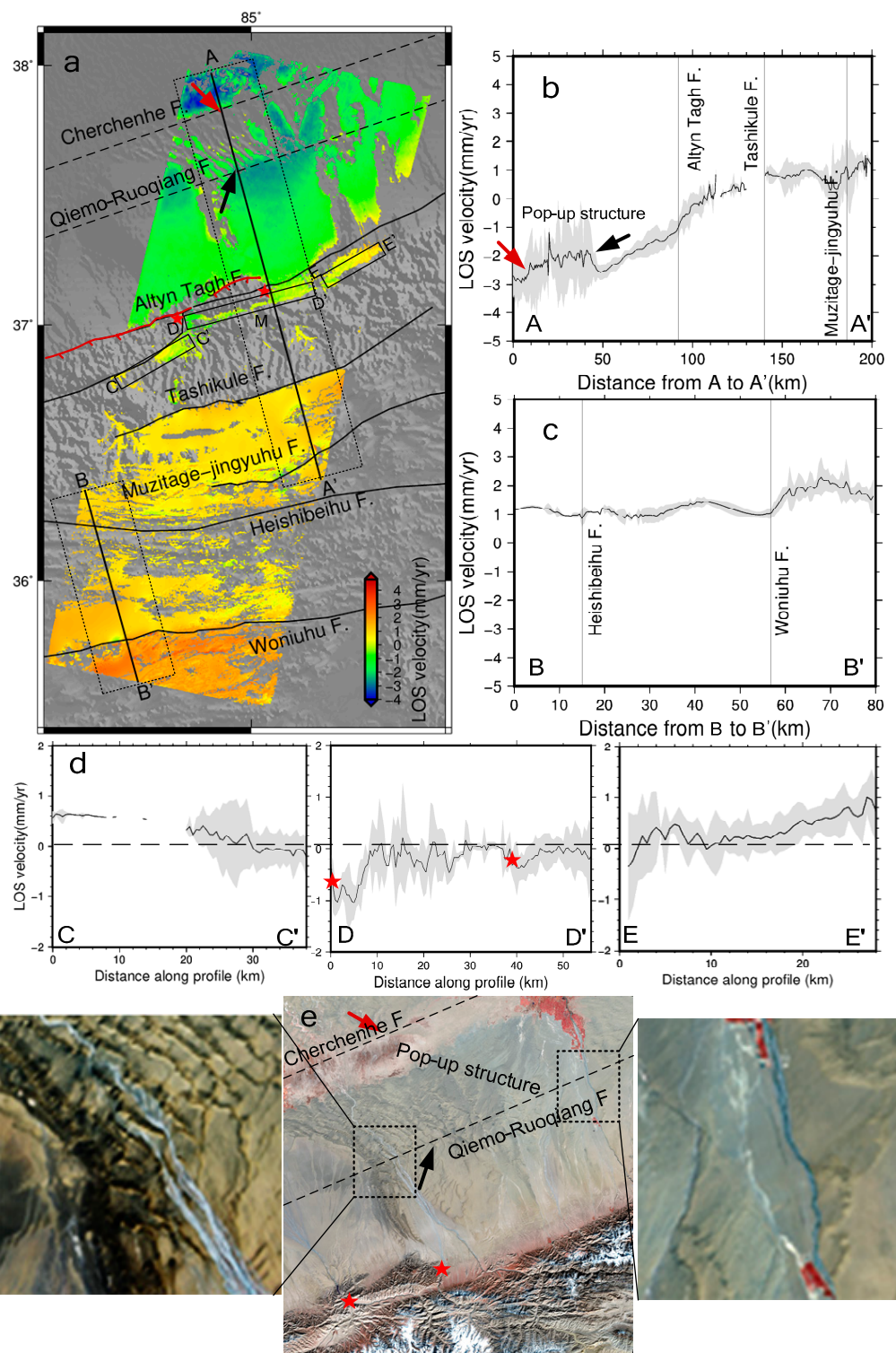


Figure 3. (a) Line-of-sight (LOS) velocity field of track 391. Black solid lines represent fault traces. Red solid lines represent thrust faults located at the northern front of ATF (Xu et al. [67]). Positive motion is toward the satellite. The red arrow shows the south dipping thrust and the black arrow shows the north dipping thrust south of the Tarim basin. AA' and BB' are described in (b,c). Red stars indicate sub-branchpoints of the ATF: Meletche outlet and Dalaku'an outlet. LOS velocity profile (dark line) with 2σ deviation (gray area) of (b) AA', (c) BB', and (d) CC', DD', and EE', which parallel the ATF in (a). (e) ETM 15 m resolution false color synthesis image, stars and arrows as in (a), dot lines are two traces of the Pop-up structure.

The deformation field in the study area is dominated by lateral shear, which is driven by the strong north–south squeezing energy of the Indian plate and Tarim Basin, producing a cluster of wrenching NEE subsidiary faults. The Tashikule, Muzitage-jingyuhu, Heishibeihu, and Woniuhu Faults are almost parallel to the ATF (Figure 4). South of the ATF, the total displacement rate is likely divided among the ATF and four subsidiary faults. The LOS velocity field (Figure 3a) and profiles (Figure 3b,c) show that the velocity values of the Heishibeihu Fault are small and those of the other three subsidiary faults are generally larger (up to 0.5–0.8 mm/y). The tectonic activity on the four subsidiary faults was generally mild in comparison with the ATF.

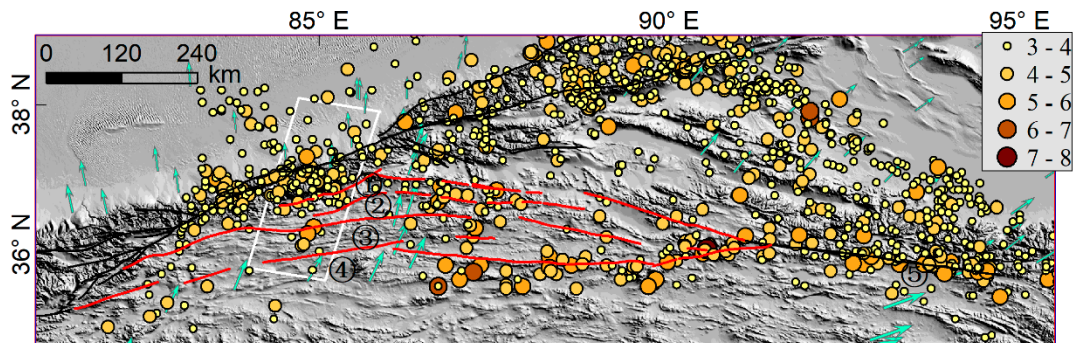


Figure 4. The four subsidiary faults (red lines), ① Tashikule, ② Muzitage-jingyuhu, ③ Heishibeihu, and ④ Woniuhu, and ⑤ the EKLf. Solid circles show earthquakes with magnitudes ≥ 3.0 from 1966 to 2020; earthquake data were downloaded from <http://data.earthquake.cn/data/index.jsp> (accessed on 10 June 2020). The faults were based on the work of Xu et al. [48]. Green arrows are GPS stations from Wang et al. [18]. The white frame denotes the study area.

3.2. Displacement Modeling

To interpret the characteristics of the LOS velocity map, we used a 2D screw dislocation model [68] (Equation (1)) to invert the fault-parallel slip rate and locking depth. Using single-fault geometry, this approach models the fault as a buried infinite screw dislocation in a homogeneous, isotropic, elastic half-space where aseismic slip occurs at a rate (V_0) below the locking depth (D) during the interseismic period. $V(x)$ is the displacement at a distance x perpendicular to the fault trace:

$$V(x) = (V_0/\pi) \times \arctan(x/D) \quad (1)$$

We assumed that LOS deformation is a combination of parallel fault deformation and vertical deformation, ignoring normal fault deformation. Under this assumption, the converted displacement in the LOS direction was decomposed into a horizontal displacement parallel to the fault. Here, we only considered horizontal displacement. The ATF is dominated by left-lateral strike-slip movements accompanied by extremely small thrusting motions [14,15,17,18]. The main error source remaining in the velocities was related to the residual turbulent atmosphere and residual orbit in the interferograms. We used a Monte Carlo simulation approach to account for uncertainties in InSAR velocities. The fault-parallel velocities are perturbed up to a value of 1σ uncertainties of the data using a normal noise distribution. Subsequently, a simulated annealing method was used to obtain the best curve-fitting solution (Figure 5). Five hundred Monte Carlo simulations were implemented for each profile, from which the fault slip rate, locking depth, and uncertainties were derived. The best-fit model corresponding to the minimum of root mean square (RMS) misfit estimated a 6.3 ± 1.4 mm/y slip rate and a 16.3 ± 2.5 km locking depth. The slip rate of the ATF was a little lower than the previously reported values in Table 1. The total slip rate of the four subsidiary faults was 5.9 ± 2.8 mm/y in $84.5\text{--}85.5^\circ\text{E}$ and the eastward decomposition of the slip rate was 5.7 ± 2.7 mm/y.

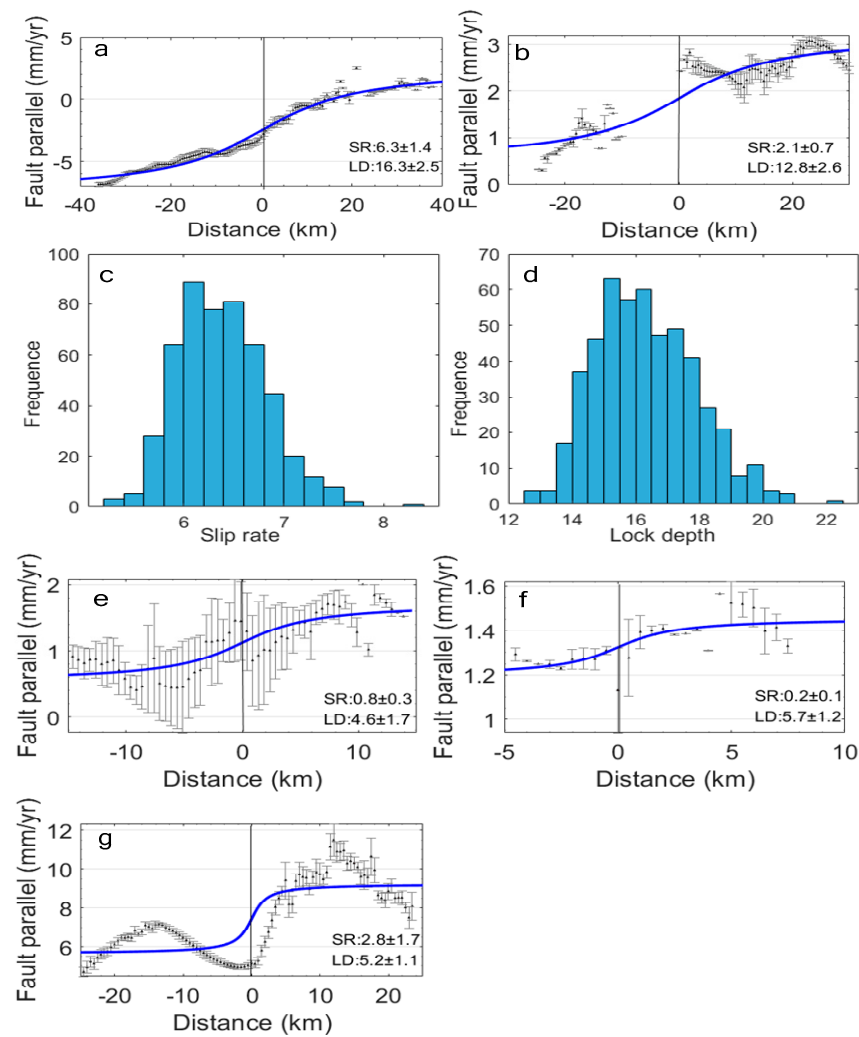


Figure 5. Interseismic fault-parallel InSAR velocities (black points) calculated using the average rates and standard deviation of all the pixels (error bars) within a 20 km-wide bin along the profile. Blue lines correspond to the best fitting model using the 2D screw dislocation model [68], with values of locking depth and slip rate and their uncertainties labeled. Diagrams (a,c,d) show the results from the Monte Carlo error analysis of the ATF and the higher frequencies of the slip rate and depth concentrate at 6.3 mm/y and 16.3 km, respectively. The best-fit slip rates (SR) and locking depths (LD) and their uncertainties for the Tashikule, Muzitage-jingyuhu, Heishibeihu, and Woniuhu Faults are 2.1 ± 0.7 mm/y and 12.8 ± 2.6 km (b), 0.8 ± 0.3 mm/y and 4.6 ± 1.7 km (e), 0.2 ± 0.1 mm/y and 5.7 ± 1.2 km (f), 2.8 ± 1.7 mm/y and 5.2 ± 1.1 km (g), respectively.

Table 1. Parameters of the ATF in recent studies.

Reference	Slip Rate (mm/y)	Locking Depth (km)	Longitude
Zhu et al. [15]	8.0 ± 0.7	14.5 ± 3.0	84.0–85.5°E
Zheng et al. [16]	8.1 ± 0.7	13.0 ± 4.0	86°E
Daout et al. [20]	10.5	17	83.5–87.0°E
Shen et al. [69]	12.3 ± 1.5	10.0 ± 2.3	85.3°E
Wang et al. [18]	11	-	83°E
He et al. [14]	9.0 ± 4.0	14.5	86°E
Li et al. [17]	8.5 ± 1.0	23.1 ± 9.8	86°E
Xu et al. [70]	7.4 ± 0.8	18.0	83.0–84.0°E
This paper	6.3 ± 1.4	16.3 ± 2.5	84.5–85.5°E

4. Discussion

A surface velocity gradient occurs in the NEE direction along the active faults (Figure 3). Surface displacements suggest that the strain is localized along the ATF zone and is partitioned at the subsidiary faults. The sharp deformation gradient is the Tanan pop-up structure identified by Zhou and Liu [65,66] along the southern rim of the Tarim Basin. The structure is controlled by the south-dipping Cherchenhe Fault and north-dipping Qiemo-ruoqiang Fault. These are deep basement faults formed during the Early Paleozoic that affect the overlying sedimentary distribution [71]. The faults show no clear surface traces in the ETM images (Figure 3e).

The slip rate of ATF was lower than the other geodetic inversion results (Table 1), and the discrepancy was mainly due to the distance of the constraint data to the ATF in the southern direction. The distance in this paper is 40 km, which excludes the cluster of wrenching NEE subsidiary faults almost paralleling ATF. In other studies, the distance is >100 km. This means the strain is distributed between the ATF and the four subsidiary faults in our result, while the previous result showed the strain only located on the ATF. Previous studies showed that deformation is broadly distributed throughout TP [27,32]. Broadly distributed deformation also accumulates strain energy on faults within the blocks [72]. Our result supported the distributed deformation mode by geophysical observation. Earthquakes with magnitudes of no less than 3.0 occurred from 1966 to 2020, including two M 5.3 earthquakes (Figure 4), which implies that strain energy accumulated on the four subsidiary faults. A shear strain rate of 18–24 nanostrain/y of GPS was found in the four fault zones, and the GPS parallel velocity profile H showed a significant gradient across the four faults [18]. The seismic and GPS evidence also showed that the dominant deformation is distributed shear deformation and also proved our result is correct. The eastern velocity component difference between the two GPS stations (GRUB and J343; Figure 1) was 5.3 mm/y. The best-fit total slip rate of the four subsidiary faults is 5.9 ± 2.8 mm/y in the section 84.5–85.5°E and the eastward decomposition of the slip rate is 5.7 ± 2.7 mm/y. The modeling slip rate in this paper is consistent with the GPS results. This consistency indicates the accuracy of the slip rate of the subsidiary faults, as well as disregarding deformation produced by the subsidiary faults in the study area which will significantly over estimate the slip rate of ATF.

The traces of the four subsidiary faults were the western splay of the EKLF (Figure 4), and in addition to the Tashikule Fault, the locking depths of the other three subsidiary faults were approximately 5.0 km. The locking depth is 6.3 ± 3.6 km across the splay segment of the EKLF [47]. The consistency of the locking depth also implied our result is accurate. The amalgamation of the traces of the subsidiary faults with the EKLF (Figure 4) illustrates to a certain extent that they have the same source of deformation, while the displacements of the subsidiary faults are tectonic deformations and not permafrost freeze–thaw deformation. The locking depth of Tashikule Fault (12.8 ± 2.6 km) is closer to that of the ATF (16.3 ± 2.5 km). A shallow locking depth, indicating a localized gradient deformation, and a deep locking depth are consistent with spread-out gradients of deformation, which stand out in observations (Figure 5). The across-fault velocity gradients (Figure 3) suggested that the strain was partitioned between the south of ATF and the subsidiary faults. Such strain partitioning on numerous discontinuous faults is a signature of an unstable evolving plate boundary [73]. The Bayan Har block is the largest tectonic block and its range is delineated by the Ganzi–Yushu–Xianshuihe fault to the southwest, the Longmenshan and Jiuzhaigou–Huya faults to the east, and the East Kunlun fault to the northeast. These block boundaries attract broad attention from Earth scientists because more than a dozen strong earthquakes occurred in the last half century. However, the Heishibeihu Fault (one of four subsidiary faults) determined to be the northwest margin of the Bayan Har block [43–45], has been neglected as an interblock subsidiary fault. The strain distributed between the ATF and the four subsidiary faults in our result confirmed that the subsidiary faults accommodate oblique convergence. Based on the snapshot of evolution of a distributed plate boundary [73] and the traces amalgamation of the subsidiary faults with the EKLF (delineated

Bayan Har plate boundary to the northeast), we can infer that the four subsidiary faults are the evolving plate boundary of the Bayan Har block to the northwest. The evolving plate northwest boundary of the Bayan Har block may provide insight into understanding the deformation behavior of the plateau.

Other continental strike-slip faults (such as the Kunlun Fault, the San Andreas Fault and the North Anatolian Fault) have numerous catastrophic earthquakes, conversely, only a minor level of seismicity has been detected along the entire active strike-slip ATF over nearly 100 years [9]. Since there have been no catastrophic earthquakes along the ATF, a high slip rate would accommodate a large part of the India–Asia convergence. In reality, the ATF does not have rapid slipping (Table 1) and the slip rate is even lower in our result. The low slip rate indicates that the ATF played only a secondary role in the northeastward extrusion of material in the TP, with most of the extrusion occurring in the interior of the plateau [15]. The reason that the slip rate of the ATF was a little lower than the previously reported values in Table 1 is that the subsidiary faults accommodate part of the strain in the study area. Therefore, our results are close to the continuum deformation models requiring low fault slip rates.

The profile in Figure 3d shows that the LOS velocity is generally reduced near the sub-branchpoints (indicated by two red stars), where two branch thrust faults are located south of the ATF, as shown in Figure 3a. In this region, a little energy is transferred to the thrusts that build the mountains. Previous studies [10,48] reported the same results—the slip rate decreased at the branchpoints along the ATF.

5. Conclusions

We constructed an LOS velocity map covering a $100 \text{ km} \times 300 \text{ km}$ area by a series of refined data processing approaches. The surface displacement gradient faults showed that the strain not only was localized along the ATF but also accumulated on the four subsidiary faults. The simple 2D kinematic fault model showed that the oblique movement is partitioned between a left-lateral slip at a rate of $6.3 \pm 1.4 \text{ mm/y}$ on the ATF and $5.9 \pm 2.8 \text{ mm/y}$ on the four subsidiary faults. The discrepancy of the slip rate on the ATF between our result and other space geodesy techniques at approximately 10 mm/y (Table 1) resulted due to four subsidiary faults accommodating the oblique movement. Meanwhile, the low slip rate of the ATF indicates that the ATF does not drive the northeastward extrusion of material, with most of the extrusion occurring in the eastern interior of the plateau and the four subsidiary faults localizing the oblique convergence partitioned in the west. This can reasonably explain why catastrophic earthquakes and rapid slip do not occur all over along the ATF and also show that deformation is broadly distributed in TP, and the deformation pattern is close to the continuum deformation models.

Based on the four subsidiary faults accommodating the oblique movement and the traces amalgamation with the EKLF (delineated Bayan Har plate boundary to the northeast), we concluded guardedly that the four subsidiary faults are the evolving plate boundary of the Bayan Har block to the northwest; this may be provide insight into understanding the evolution process of the TP.

Supplementary Materials: The following supporting information can be downloaded at: <https://www.mdpi.com/article/10.3390/rs15215195/s1>, Figure S1. Comparison of the co-registration accuracy in the (a) range and (b) azimuth directions based on the digital elevation model (DEM) and coherence coefficient; Figure S2. Interferogram showing the effects of atmospheric phase screen (APS) and DEM errors and the orbital ramp; Figure S3. Profiles of the middle row of interferograms respectively, in Figure S2; Figure S4. Profiles of the DEM errors and elevation; Figure S5. Unwrapping errors detected by a phase-closure technique; Figure S6. Orbital ramps.

Author Contributions: G.Z. designed the research, processed, and analyzed the data, wrote the first draft of the manuscript, and reviewed and edited the manuscript. X.S. (Xinjian Shan) proposed crucial suggestions. C.Q. led the research work and proposed the structure of this manuscript. Y.Z. and Y.L. proposed helpful suggestions. X.S. (Xiaogang Song) reviewed and edited the manuscript. All authors have read and agreed to the published version of the manuscript.

Funding: This work was supported by the Basic Scientific Funding of the Institute of Geology, China Earthquake Administration (No. IGCEA2104).

Data Availability Statement: The AW3D30 DEM is provided by the Japan Aerospace Exploration Agency (JAXA) (<https://www.eorc.jaxa.jp/ALOS/en/aw3d30/data/index.htm>, accessed on 8 May 2016). The GACOS data can be downloaded from the website (<http://ceg-research.ncl.ac.uk/v2/gacos/>, accessed on 8 July 2016).

Acknowledgments: This work is co-supported by the National Key Research and Development Program of China (Grant No. 2019YFC1509201). The author highly appreciated Guifang's collaborating supervisor, Zhenhong Li, at Newcastle University, for his support and constructive suggestions. Envisat data were provided and copyrighted by the European Space Agency.

Conflicts of Interest: The authors declare that they have no known competing financial interest or personal relationships that could have appeared to influence the work reported in this paper.

References

1. Lin, Y.N.N.; Simons, M.; Hetland, E.A.; Muse, P.; DiCaprio, C. A multiscale approach to estimating topographically correlated propagation delays in radar interferograms. *Geochem. Geophys. Geosyst* **2010**, *11*, Q09002. [[CrossRef](#)]
2. Zhang, P.Z.; Shen, Z.; Wang, M.; Gan, W.; Burgmann, R.; Molnar, P.; Wang, Q.; Niu, Z.; Sun, J.; Wu, J.; et al. Continuous deformation of the Tibetan Plateau from global positioning system data. *Geology* **2004**, *32*, 809–812. [[CrossRef](#)]
3. Wang, Q.; Zhang, P.Z.; Freymueller, J.T.; Bilham, R.; Larson, K.M.; Lai, X.A.; You, X.; Niu, Z.; Wu, J.; Li, Y.; et al. Present-Day Crustal Deformation in China Constrained by Global Positioning System Measurements. *Science* **2001**, *294*, 574–577. [[CrossRef](#)]
4. England, P.; Molnar, P. The field of crustal velocity in Asia calculated from Quaternary rates of slip on faults. *Geophys. J. Int.* **1997**, *130*, 551–582. [[CrossRef](#)]
5. Tapponnier, P.; Zhiqin, X.; Roger, F.; Meyer, B.; Arnaud, N.; Wittlinger, G.; Yang, J. Oblique stepwise rise and growth of the Tibet plateau. *Science* **2001**, *294*, 1671–1677. [[CrossRef](#)] [[PubMed](#)]
6. Williams, S.; Bock, Y.; Fang, P. Integrated satellite interferometry: Tropospheric noise, GPS estimates and implications for interferometric synthetic aperture radar products. *J. Geophys. Res. Solid Earth* **1998**, *103*, 27051–27067. [[CrossRef](#)]
7. Zhao, J.; Yuan, X.; Liu, H.; Kumar, P.; Pei, S.; Kind, R.; Zhang, Z.; Teng, J.; Ding, L.; Gao, X.; et al. The boundary between the Indian and Asian tectonic plates below Tibet. *Proc. Natl. Acad. Sci. USA* **2010**, *107*, 11229–11233. [[CrossRef](#)] [[PubMed](#)]
8. Xiao, Q.; Yu, G.; Liu-Zeng, J.; Oskin, M.E.; Shao, G. Structure and geometry of the Aksay restraining double bend along the Altyn Tagh Fault, northern Tibet, imaged using magnetotelluric method. *Geophys. Res. Lett.* **2017**, *44*, 4090–4097. [[CrossRef](#)]
9. Shen, Z.K.; Wang, M.; Li, Y.; Jackson, D.D.; Yin, A.; Dong, D.; Fang, P. Crustal deformation along the Altyn Tagh fault system, western China, from GPS. *J. Geophys. Res. Solid Earth* **2001**, *106*, 30607–30621. [[CrossRef](#)]
10. Mériaux, A.-S.; Ryerson, F.J.; Tapponnier, P.; Van der Woerd, J.; Finkel, R.C.; Xu, X.; Xu, Z.; Caffee, M.W. Rapid slip along the central Altyn Tagh Fault: Morphochronologic evidence from Cherchen He and Sulamu Tagh. *J. Geophys. Res. Atmos.* **2004**, *109*, B6. [[CrossRef](#)]
11. Mériaux, A.-S.; Tapponnier, P.; Ryerson, F.J.; Xiwei, X.; King, G.; Van der Woerd, J.; Finkel, R.C.; Haibing, L.; Caffee, M.W.; Zhiqin, X.; et al. The Aksay segment of the northern Altyn Tagh fault: Tectonic geomorphology, landscape evolution, and Holocene slip rate. *J. Geophys. Res. Solid Earth* **2005**, *110*, 229–246. [[CrossRef](#)]
12. Zhang, P.-Z.; Molnar, P.; Xu, X. Late Quaternary and present-day rates of slip along the Altyn Tagh Fault, northern margin of the Tibetan Plateau. *Tectonics* **2007**, *26*, TC5010. [[CrossRef](#)]
13. Gold, R.D.; Cowgill, E.; Arrowsmith, J.R.; Gosse, J.; Chen, X.; Wang, X.F. Riser diachroneity, lateral erosion, and uncertainty in rates of strike-slip faulting: A case study from Tuzidun along the Altyn Tagh Fault, NW China. *J. Geophys. Res. Solid Earth* **2009**, *114*, B04401. [[CrossRef](#)]
14. He, J.; Vernant, P.; Chéry, J.; Wang, W.; Lu, S.; Ku, W.; Xia, W.; Bilham, R. Nailing down the slip rate of the Altyn Tagh fault. *Geophys. Res. Lett.* **2013**, *40*, 5382–5386. [[CrossRef](#)]
15. Zhu, S.; Xu, C.; Wen, Y.; Liu, Y. Interseismic Deformation of the Altyn Tagh Fault Determined by Interferometric Synthetic Aperture Radar (InSAR) Measurements. *Remote Sens.* **2016**, *8*, 233. [[CrossRef](#)]
16. Zheng, G.; Wang, H.; Wright, T.J.; Lou, Y.; Zhang, R.; Zhang, W.; Shi, C.; Huang, J.; Wei, N. Crustal Deformation in the India-Eurasia Collision Zone From 25 Years of GPS Measurements. *J. Geophys. Res. Solid Earth* **2017**, *122*, 9290–9312. [[CrossRef](#)]
17. Li, Y.; Shan, X.; Qu, C.; Liu, Y.; Han, N. Crustal Deformation of the Altyn Tagh Fault Based on GPS. *J. Geophys. Res. Solid Earth* **2018**, *123*, 10309–10322. [[CrossRef](#)]
18. Wang, M.; Shen, Z.-K. Present-Day Crustal Deformation of Continental China Derived from GPS and its Tectonic Implications. *J. Geophys. Res. Solid Earth* **2020**, *125*, e2019JB018774. [[CrossRef](#)]
19. Peltzer, G.; Tapponnier, P.; Armijo, R. Magnitude of late Quaternary left-lateral displacements along the north edge of Tibet. *Science* **1989**, *8*, 1285–1289. [[CrossRef](#)]
20. Daout, S.; Doin, M.P.; Peltzer, G.; Lasserre, C.; Socquet, A.; Volat, M.; Sudhaus, H. Strain Partitioning and Present-Day Fault Kinematics in NW Tibet From Envisat SAR Interferometry. *J. Geophys. Res. Solid Earth* **2018**, *123*, 2462–2483. [[CrossRef](#)]

21. Qiu, J.; Zhu, L.; Wang, S. Study on the Contemporary Tectonic Deformation Pattern of the Middle Altyn Tagh Fault Zone as Revealed by InSAR Measurements. *J. Geod. Geodyn.* **2018**, *38*, 783–786.
22. Avouac, J.P.; Tapponnier, P.; Bai, M.; You, H.; Wang, G. Active thrusting and folding along the northern Tien Shan and Late Cenozoic rotation of the Tarim relative to Dzungaria and Kazakhstan. *J. Geophys. Res. Solid Earth* **1993**, *98*, 6755–6804. [[CrossRef](#)]
23. Mériaux, A.-S.; Van der Woerd, J.; Tapponnier, P.; Ryerson, F.J.; Finkel, R.C.; Lasserre, C.; Xu, X. The Pingding segment of the Altyn Tagh Fault (91°E): Holocene slip-rate determination from cosmogenic radionuclide dating of offset fluvial terraces. *J. Geophys. Res. Solid Earth* **2012**, *117*, B09406. [[CrossRef](#)]
24. Tapponnier, P.; Peltzer, G.L.; Le Dain, A.Y.; Armijo, R.; Cobbold, P. Propagating extrusion tectonics in Asia: New insights from simple experiments with plasticine. *Geology* **1982**, *10*, 611–616. [[CrossRef](#)]
25. Replumaz, A.; Tapponnier, P. Reconstruction of the deformed collision zone Between India and Asia by backward motion of lithospheric blocks. *J. Geophys. Res. Atmos.* **2003**, *108*, 2285. [[CrossRef](#)]
26. Zheng, W.J.; Zhang, P.Z.; Yuan, D.Y.; Zheng, D.W.; Li, C.; Zhang, P.; Yin, J.; Min, W.; Heermance, R.; Chen, J. Deformation on the northern of the Tibetan plateau from GPS measurement and geologic rates of Late Quaternary along the major fault. *Chin. J. Geophys.* **2009**, *52*, 2491–2508.
27. Royden, L.H.; Burchfiel, B.C.; King, R.W.; Wang, E.; Chen, Z.; Shen, F.; Liu, Y. Surface Deformation and Lower Crustal Flow in Eastern Tibet. *Science* **1997**, *276*, 788–790. [[CrossRef](#)]
28. Houseman, G.; England, P. A lithospheric-thickening model for the Indo-Asian collision. *World Reg. Geol.* **1996**, *1*, 1–17.
29. Avouac, J.-P.; Tapponnier, P. Kinematic model of active deformation in central Asia. *Geophys. Res. Lett.* **1993**, *20*, 895–898. [[CrossRef](#)]
30. Thatcher, W. How the Continents Deform: The Evidence from Tectonic Geodesy. *Annu. Rev. Earth Planet. Sci.* **2009**, *37*, 237–262. [[CrossRef](#)]
31. Weholt, L.A. Dynamics of the India-Eurasia collision zone. *Transl. World Seismol.* **2003**, *2*, 34–56.
32. England, P.; Molnar, P. Late Quaternary to decadal velocity fields in Asia. *J. Geophys. Res. Solid Earth* **2005**, *110*, B12401. [[CrossRef](#)]
33. England, P.; Jackson, J. Active Deformation of the Continents. *Annu. Rev. Earth Planet. Sci.* **1989**, *17*, 197–226. [[CrossRef](#)]
34. Meade, B.J. Present-day kinematics at the India-Asia collision zone. *Geology* **2007**, *35*, 81–84. [[CrossRef](#)]
35. Thatcher, W. Microplate model for the present-day deformation of Tibet. *J. Geophys. Res. Solid Earth* **2007**, *112*, 534–535. [[CrossRef](#)]
36. Wang, W.; Qiao, X.; Yang, S.; Wang, D. Present-day velocity field and block kinematics of Tibetan Plateau from GPS measurements. *Geophys. J. Int.* **2016**, *208*, 1088–1102. [[CrossRef](#)]
37. Li, Y.; Shan, X.; Qu, C.; Zhang, Y.; Song, X.; Jiang, Y.; Zhang, G.; Nocquet, J.M.; Gong, W.; Gan, W.; et al. Elastic block and strain modeling of GPS data around the Haiyuan-Liupanshan fault, northeastern Tibetan Plateau. *J. Asian Earth Sci.* **2017**, *150*, 87–97. [[CrossRef](#)]
38. Song, X.; Jiang, Y.; Shan, X.; Gong, W.; Qu, C.A. Fine Velocity and Strain Rate Field of Present-Day Crustal Motion of the Northeastern Tibetan Plateau Inverted Jointly by InSAR and GPS. *Remote Sens.* **2019**, *11*, 435. [[CrossRef](#)]
39. Zhang, L.; Cao, D.; Zhang, J.; Sui, L. Interseismic Fault Movement of Xianshuihe Fault Zone Based on Across-Fault Deformation Data and InSAR. *Pure Appl. Geophys.* **2019**, *176*, 649–667. [[CrossRef](#)]
40. Wang, H.; Zhang, G.M.; Wu, Y.; Ma, H.S. The Deformation of Active Crustal-Blocks on the Chinese Mainland and Its Relation with Seismic Activity. *Earthq. Res. China* **2003**, *19*, 243–254.
41. Loveless, J.P.; Meade, B.J. Partitioning of localized and diffuse deformation in the Tibetan Plateau from joint inversions of geologic and geodetic observations. *Earth Planet. Sci. Lett.* **2011**, *303*, 11–24. [[CrossRef](#)]
42. Yue, H.; Shen, Z.K.; Zhao, Z.; Wang, T.; Cao, B.; Li, Z.; Bao, X.; Zhao, L.; Song, X.; Ge, Z.; et al. Rupture process of the 2021 M7.4 Maduo earthquake and implication for deformation mode of the Songpan-Ganzi terrane in Tibetan Plateau. *Proc. Natl. Acad. Sci. USA* **2022**, *119*, e2116445119. [[CrossRef](#)] [[PubMed](#)]
43. Yao, S.; Cheng, J.; Yao, Q.; Zhang, J. Preliminary Study on the Division of the Bayan Har Block Using GPS Data and a Block Model and the Tectonic Implications of the Division. *Chin. Earthq. Eng. J.* **2018**, *5*, 175–184.
44. Dong, P.; Cheng, H.; Shi, Y.; Liu, C.; Qiao, X. Numerical inversion of regional initial tectonic stress based on Monte Carlo method—A case study of Bayan Har block. *Chin. J. Geophys.* **2019**, *8*, 80–92.
45. Sun, Y.; Fan, T.; Zhou, C.; Wu, Z. The Evolution of Stress and Strain around the Bayan Har Block in the Tibetan Plateau. *J. Earthq.* **2015**, *2015*, 971628. [[CrossRef](#)]
46. Zhao, D.; Qu, C.; Shan, X.; Bürgmann, R.; Gong, W.; Zhang, G. Spatiotemporal Evolution of Postseismic Deformation Following the 2001 Mw7.8 Kokoxili, China, Earthquake from 7 Years of InSAR Observations. *Remote Sens.* **2018**, *10*, 1988. [[CrossRef](#)]
47. Zhao, D.; Qu, C.; Bürgmann, R.; Gong, W.; Shan, X.; Qiao, X.; Zhao, L.; Chen, H.; Liu, L. Large-Scale Crustal Deformation, Slip-Rate Variation, and Strain Distribution Along the Kunlun Fault (Tibet) from Sentinel-1 InSAR Observations (2015–2020). *J. Geophys. Res. Solid Earth* **2022**, *127*, e2021JB022892. [[CrossRef](#)]
48. Xu, X.W.; Han, Z.J.; Yang, X.P.; Zhang, S.M.; Yu, G.H.; Zhou, B.G.; Li, F.; Chen, G.H.; Ran, Y.K. *Seismotectonic Map in China and its Adjacent Regions*; Beijing Seismological Press: Beijing, China, 2016. (In Chinese)
49. Cavalié, O.; Lasserre, C.; Doin, M.P.; Peltzer, G.; Sun, J.; Xu, X.; Shen, Z.K. Measurement of interseismic strain across the Haiyuan fault (Gansu, China), by InSAR. *Earth Planet. Sci. Lett.* **2008**, *275*, 246–257. [[CrossRef](#)]
50. Jolivet, R.; Lasserre, C.; Doin, M.P.; Guillaso, S.; Peltzer, G.; Dailu, R.; Sun, J.; Shen, Z.K.; Xu, X. Shallow creep on the Haiyuan Fault (Gansu, China) revealed by SAR Interferometry. *J. Geophys. Res. Solid Earth* **2012**, *117*, B06401. [[CrossRef](#)]

51. Bekaert, D.P.S.; Hooper, A.; Wright, T.J. A spatially-variable power-law tropospheric correction technique for InSAR data. *J. Geophys. Res. Solid Earth* **2015**, *120*, 1345–1356. [[CrossRef](#)]
52. Webley, P.W.; Bingley, R.M.; Dodson, A.H.; Wadge, G.; Waugh, S.J.; James, I.N. Atmospheric water vapour correction to InSAR surface motion measurements on mountains: Results from a dense GPS network on Mount Etna. *Phys. Chem. Earth* **2002**, *27*, 363–370. [[CrossRef](#)]
53. Doin, M.P.; Lasserre, C.; Peltzer, G.; Cavalié, O.; Doubre, C. Corrections of stratified tropospheric delays in SAR interferometry: Validation with global atmospheric models. *J. Appl. Geophys.* **2009**, *69*, 35–50. [[CrossRef](#)]
54. Jolivet, R.; Grandin, R.; Lasserre, C.; Doin, M.P.; Peltzer, G. Systematic InSAR tropospheric phase delay corrections from global meteorological reanalysis data. *Geophys. Res. Lett.* **2011**, *38*, L17311. [[CrossRef](#)]
55. Jolivet, R.; Agram, P.S.; Lin, N.Y.; Simons, M.; Doin, M.P.; Peltzer, G.; Li, Z. Improving InSAR geodesy using Global Atmospheric Models. *J. Geophys. Res. Solid Earth* **2014**, *119*, 2324–2341. [[CrossRef](#)]
56. Yu, C.; Penna, N.T.; Li, Z. Generation of real-time mode high-resolution water vapor fields from GPS observations. *J. Geophys. Res. Atmos.* **2017**, *122*, 2008–2025. [[CrossRef](#)]
57. Ducret, G.; Doin, M.P.; Grandin, R.; Lasserre, C.; Guillaso, S. DEM Corrections Before Unwrapping in a Small Baseline Strategy for InSAR Time Series Analysis. *Geosci. Remote Sens. Symp.* **2014**, *11*, 696–700. [[CrossRef](#)]
58. Biggs, J.; Wright, T.; Lu, Z.; Parsons, B. Multi-interferogram method for measuring interseismic deformation: Denali fault, Alaska. *Geophys. J. Int.* **2007**, *170*, 1165–1179. [[CrossRef](#)]
59. Kohlhase, A.O.; Kroes, R.; D’Amico, S. Interferometric Baseline Performance Estimations for Multistatic Synthetic Aperture Radar Configurations Derived from GRACE GPS Observations. *J. Geod.* **2006**, *80*, 28–39. [[CrossRef](#)]
60. Hanssen, R. *Radar Interferometry: Data Interpretation and Error Analysis, 1st ed*; Kluwer Academic Publishers: Dordrecht, The Netherlands, 2001; Volume 2.
61. Li, Z.; Fielding, E.J.; Cross, P.; Preusker, R. Advanced InSAR atmospheric correction: MERIS/MODIS combination and stacked water vapour models. *Int. J. Remote Sens.* **2009**, *30*, 3343–3363. [[CrossRef](#)]
62. Wen, Y.; Li, Z.; Xu, C.; Ryder, I.; Bürgmann, R. Postseismic motion after the 2001 MW7.8 Kokoxili earthquake in Tibet observed by InSAR time series. *J. Geophys. Res. Solid Earth* **2012**, *117*, B08405. [[CrossRef](#)]
63. Zhang, L.; Ding, X.; Lu, Z.; Jung, H.S.; Hu, J.; Feng, G. A Novel Multitemporal InSAR Model for Joint Estimation of Deformation Rates and Orbital Errors. *IEEE Trans. Geosci. Remote Sens.* **2014**, *52*, 3529–3540. [[CrossRef](#)]
64. Heresh, F.; Falk, A. InSAR uncertainty due to orbital errors. *Geophys. J. Int.* **2014**, *199*, 549–560.
65. Zhou, X.Y.; Luo, J.; Wang, Q. Structural features and petroleum geology of the fold-thrust belt in the southern Tarim basin, China. *Sci. China (Earth Sci.)* **2004**, *47*, 66–73. [[CrossRef](#)]
66. Liu, X.W.; Zheng, J.J.; Yang, X.; Sun, G.Q.; Su, L.; Wang, Y.D. Sedimentology Revealment to Meso-Cenozoic Tectonic Movement Process of Altun Strike-slip Fault. *Nat. Gas. Geosci.* **2012**, *23*, 119–128.
67. Xu, X.; Wang, F.; Zheng, R.; Chen, W.; Ma, W.; Yu, G.; Chen, G.; Tapponnier, P.; Van Der Woerd, J.; Meriaux, A.S.; et al. Late Quaternary sinistral slip rate along the Altyn Tagh fault and its structural transformation model. *Sci. China* **2005**, *48*, 384–397. [[CrossRef](#)]
68. Savage, J.C.; Burford, R.O. Geodetic determination of relative plate motion in central California. *J. Geophys. Res.* **1973**, *78*, 832–845. [[CrossRef](#)]
69. Shen, L.; Hooper, A.; Elliott, J. A spatially-varying scaling method for inSAR tropospheric corrections using a high-resolution weather model. *J. Geophys. Res. Solid Earth* **2019**, *124*, 4051–4068. [[CrossRef](#)]
70. Xu, C.J.; Zhu, S. Temporal and spatial movement characteristics of the Altyn Tagh fault inferred from 21 years of InSAR observations. *J. Geod.* **2019**, *93*, 1147–1160. [[CrossRef](#)]
71. Xie, X.O.; Wu, Q.Z.; Gan, Y.; Lu, H.F. Hydrocarbon accumulation and structural characteristics of compress-wrench fault belts in Tarim basin. *Acta Pet. Sin.* **1997**, *18*, 13–17.
72. Wang, M.; Wang, F.; Jiang, X.; Tian, J.; Li, Y.; Sun, J.; Shen, Z.K. GPS determined coseismic slip of the 2021 Mw7.4 Maduo, China, earthquake and its tectonic implication. *Geophys. J. Int.* **2021**, *228*, 2048–2055. [[CrossRef](#)]
73. Dalaison, M.; Jolivet, R.; Le Pourhiet, L. A snapshot of the long-term evolution of a distributed tectonic plate boundary. *Sci. Adv.* **2023**, *9*, eadd7235. [[CrossRef](#)] [[PubMed](#)]

Disclaimer/Publisher’s Note: The statements, opinions and data contained in all publications are solely those of the individual author(s) and contributor(s) and not of MDPI and/or the editor(s). MDPI and/or the editor(s) disclaim responsibility for any injury to people or property resulting from any ideas, methods, instructions or products referred to in the content.